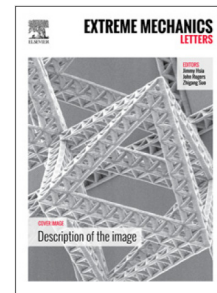# Journal Pre-proof

Vibration behavior and excitation mechanism of ultra-stretchable triboelectric nanogenerator for wind energy harvesting

Zewei Ren, Ziming Wang, Fan Wang, Site Li, Zhong Lin Wang

Please cite this article as: Z. Ren, Z. Wang, F. Wang et al., Vibration behavior and excitation mechanism of ultra-stretchable triboelectric nanogenerator for wind energy harvesting, *Extreme Mechanics Letters* (2021), doi: https://doi.org/10.1016/j.eml.2021.101285.

This is a PDF file of an article that has undergone enhancements after acceptance, such as the addition of a cover page and metadata, and formatting for readability, but it is not yet the definitive version of record. This version will undergo additional copyediting, typesetting and review before it is published in its final form, but we are providing this version to give early visibility of the article. Please note that, during the production process, errors may be discovered which could affect the content, and all legal disclaimers that apply to the journal pertain.

Vibration behavior and excitation mechanism of ultra-stretchable triboelectric nanogenerator for wind energy harvesting

Zewei Ren[1,2], Ziming Wang[1,2], Fan Wang[1,2], Site Li[4], Zhong Lin Wang[1,2,3]*

[1] CAS Center for Excellence in Nanoscience, Beijing Key Laboratory of Micro-nano Energy and Sensor, Beijing Institute of Nanoenergy and Nanosystems, Chinese Academy of Sciences, Beijing 100083, P. R. China.

[2] School of Nanoscience and Technology, University of Chinese Academy of Sciences, Beijing, 100049, China.

[3] School of Material Science and Engineering, Georgia Institute of Technology, Atlanta, Georgia 30332-0245, USA.

[4] Department of Chemistry, Carnegie Mellon University, Pittsburgh, Pennsylvania 15213, USA.

Correspondence and requests for materials should be addressed to Z.L. Wang (Email: zhong.wang@mse.gatech.edu).

Abstract

Wind is one of the cleanest energy sources, and various wind energy harvesters have been proposed. Here, we study the vibration behavior and excitation mechanism of an ultra-stretchable electrode film, using which the fabricated TENG device if for wind energy harvesting. The motion of the ultra-stretchable film in the flow is illustrated as a coupling of vortex-induced elastic torsional deformation and pressure-driven galloping. Aerodynamic models based on structural mechanics and computational fluid dynamics (CFD) are established to systematically elaborate the deformation characteristics. On the basis of aerodynamic characteristics, perforations are developed on the electrode film as geometric optimization to enhance performance of the TENG, in which the output power has been improved for 56.3% in comparison to the original device. This work firstly demonstrates the flow-induced vibration of the ultra-stretchable film in TENG, which may paves a way for improving the design of miniature wind energy harvesters.

Introduction

Wind/airflow energy has attracted great interests and played a reasonable proportion in the current energy structure. As an alternative to fossil fuels, it is abundant, renewable and environmentally friendly without carbon emissions.[1,2] For wind energy harvesting, the wind turbine based on electromagnetic effect has been the most widely used approach.[3-5] However，these wind energy harvesters can only be installed in remote areas far away from city and buildings, due to their large volumes, complex structure and demand on the operating wind velocity.[6-8] Since the rapid expansion of mobile devices and Internet of Things, miniature energy harvesters have attracted considerable attention. With characteristics of small size, easy to carry-threat and long operational lifetime, these miniature harvesters are potentially expected to replace the conventional Li-ion battery as a better power supply. In order to implement the wind energy harvester on portable electronic devices and sensors, it is necessary to develop new design strategies and techniques to achieve miniaturization and enhanced performance.

Recently, triboelectric nanogenerator (TENG) based on coupling effect of triboelectrification and electrostatic induction has offered an unprecedented approach to collect environmental energy.[9,10,11,12] Aimed at low-frequency resources, the TENG devices have high efficiency in harvesting natural energy such as wind,[13] rain drop[14] and water wave,[15] etc. Accordingly, a series of TENG prototypes have been developed to target at wind energy harvesting. Many kinds of novel materials with characteristic of excitation response[16], flexible[17,18], fully-elastic[19-21] or ultra-stretchable[22] have been intensively studied, and various architectures like flutter[23,24], lawn structure[25], angle shape[26] and rotating disk[27] have been applied to these TENG prototypes. However, the motion behavior and dynamic characteristics of these wind energy harvesters based on TENG are rarely studied. Analysis of motion behavior and theoretical research are highly desired to realize both optimized devices and high performance.

Here, we demonstrate vibration behavior and excitation mechanism of the ultra-stretchable electrode film based on the fabricated TENG device for wind energy harvesting. In the advection, the vibration of the ultra-stretchable film is a complicated coupling between vortex-induced elastic torsional deformation and pressure-driven galloping. The excitation mechanism is fitted by aerodynamic models, as well as simulation of fluid-structure interactions based on CFD and finite element methods is introduced to attain confirmed investigation. Based on aerodynamic characteristics, perforations are developed on the electrode film as geometric optimization of the TENG device. The amount, distribution and diameter of the perforations have been systematically investigated. With developed perforations, fluid interacting with the electrode film has been more turbulent, where the convergence time of the film's vibration reduces by 25 % and vibration intensity increases by approximate 20%. Accordingly, the generated output power by the TENG is increased by 56.3%. This work systematically demonstrates flow-induced vibration of the ultra-stretchable film in TENG, which may serve as an important guidance for rational design of wind energy harvester.

Results and Discussion

Figure 1a shows schematic of the TENG device based on ultra-stretchable electrode. The device consists of the arc-shaped frameworks, two negative tribo-layer, and the compound ultra-stretchable film electrode sandwiched in them. In this device, the dielectric material fluorinated ethylene propylene (FEP) with decent electron affinity has been chosen as a negative tribo-layer. To enhance charge density on the tribo-layer during contact electrification, nanostructure on tribo surfaces of FEP has been developed by plasma etching. The ultra-stretchable elastic electrode is compounded by ultrathin Ecoflex substrate and thermoplastic polyurethanes (TPU) conductive nanofibers (NFs) mesh, where the TPU NFs have been modified by ultra-long silver nanowires (AgNWs). Since 0.5% N, N-Dimethylacetamide is added to the AgNWs modification solution, the adhesion between the NFs and AgNWs is strong. Scanning electron microscopy (SEM) images of TPU NFs mesh before and after treatment by AgNWs are shown in Figure S1a and Figure S1b, respectively. In order to attain good surface conductivity and contact electrification, the prepared AgNWs NFs mesh is attached on surfaces of Ecoflex substrate with a semi-embedded structure. Atomic force microscopy image of this ravine-like surface microstructure is shown in Figure S1c. Accordingly, with the fabrication structure like "sandwich", two TENG units are integrate in one device, as schematics and photographs exhibited in Figure S2.

The working principle of this TENG device for breeze energy harvesting can be divided into two energy conversion processes. That is, wind flow drives AgNWs NFs electrode to deform, and then the electrode's vibration lead to electric output based on contact electrification and electrostatic induction. With continuous motion of the AgNWs NFs electrode, the changed electric potential difference would be generated between AgNWs NFs electrode and FEP negative layer. Accordingly, an alternating output can be induced in the external circuit of the device, the detailed schematic of which can be found in Figure S3.

For ultra-stretchable AgNWs NFs electrode film fixed in our TENG device, the motion of which in wind flow can be defined as a complex vibration integrating torsional and heave deformation (schematic in Figure 1b). The deformation characteristics of the electrode film have been intuitively captured by high-speed camera, as shown in Figure 1c. Meanwhile, finite element methods (ANSYS) based on CFD and simulation of fluid-structure interactions are also carried out. Here, the established stimulating calculation model in the ANSYS consists of the whole TENG device not only the film, since the flow field around the film in airflow would be influenced by the other components of the device. The vibration of the film has been theoretically fitted well, under the boundary conditions after multiple adjustments

(Movie S1).

Under incident wind flow, torsional deformation of the electrode film is mainly induced by vortex shedding, while the galloping results from the change of angle of attack. To clearly reveal the vibration mechanism and motivation, status of the film changing from static to vibration in wind flow has been researched. At the initial state, owing to vortexes shedding, the trailing edge of the film would flap up and down accordingly. This elastic deformation on the trailing edge would bring about torsional motion of the entire film along its length direction, which finally gives rise to a corresponding angle of attack at the leading edge (high-speed photography in **Figure 2**a and Movie S2). Once an angle of attack is induced, a pressure difference on two surfaces of the film would generate, resulting from difference in flow velocities as illustrated by Bernoulli's principle:

$$P + \frac{1}{2} pv^2 + pgh = C \tag{1}$$

where P is pressure of the certain point in flow, v is flow velocity at the point, p is density of the flow, g is gravitational acceleration, h is height of the point and C is the constant. In this illustration, the critical angle of attack is formed at the leading edge of the film, and a corresponding pressure difference originating from velocity difference is generated on it. Due to the induced external pressure, the film would deform upwards and rebound back after collision with the arch frame, forming a reciprocating oscillation status. To verify this inference, the dynamic flow field demonstrating vibration of the film has been presented, as shown in Movie S3. Screenshot in Figure 2b exhibits vortexes shedding from the trailing edge of the film at the initial state, which is a verification of above-mentioned premise for the origin of angle of attack. Change of pressure distribution of the film at the beginning has also been attained, as shown in Figure S4 and Movie S4. Meanwhile, the enlarged images have been exhibited in Figure 2c, which is more clearly to distinguish the pressure change near the film's surface. The results demonstrate that the film starts to vibrate when the induced pressure difference beyond the film's motion inertia. The induced vibration would enhance the effect of vortex shedding, and conversely, the vibration would be intensified until reaching a dynamic balance.

To further analyze deformation of the electrode film, aerodynamic models of the film in flow field has been established. As illustrated in Figure 2d, the velocity of the inflow is U, the moving velocity of the film perpendicular to the inflow is expressed as:

$$\dot{y}(t) = \frac{dy}{dt} \tag{2}$$

The relative motion velocity of the film can be defined as U_r and the included angle α between the film's motion and inflow is demonstrated as:

$$\alpha = \tan^{-1}\left(\frac{\dot{y}(t)}{U}\right) \tag{3}$$

In this model, the airflow separates at corner point "1" and "2" of the film's cross section and tends to move horizontally along the bottom edge. The whole leeward area behind the cross section is a turbulent area. The negative pressure closed to the bottom "1-4" is higher than that in the area "2-3-4". In this case, a negative lateral force on the film would be induced when a positive angle of attack induces, which would enhance the vibration of the film. It's also noted that the vibration of the film occurs at a range of reduced frequency:

$$\frac{fD}{U} \leq 0.05 \tag{4}$$

where f is vibration frequency and D represents the thickness of the film there. Based on analysis of unsteady aerodynamic force of periodic vortex shedding, frequency of the vortex shedding can also be attained by Strouhal number in dimensionless form:

$$S = \frac{f'D}{U_\infty} \tag{5}$$

in which f' is number of the vortex per second.

Furthermore, the galloping characteristic of the film based on typical models of harmonic vibration with damping is demonstrated (Figure 2e). Based on aerodynamics, the relative velocity U_r of the film's cross section can be expressed as:

$$U_r^2 = \dot{y}^2(t) + U^2 \tag{6}$$

The lift force $L(t)$ that acted on the film unit length is:

$$L(t) = \frac{1}{2}\rho U^2 D C_y \tag{7}$$

where ρ is airflow density and C_y is the coefficient of lift, which can be specified as:

$$C_y = \frac{U_r^2}{U^2}(C_L \cos\alpha + C_D \sin\alpha) \tag{8}$$

C_L and C_D are coefficients of lift force and drag force, respectively. Here, considering δ_y and k_y respectively infer to the inherent damping of whole system and spring stiffness of the film, the motion equation of the cross section in this model can be deduced via the principle of force balance:

$$m\frac{\partial^2 y(t)}{\partial t^2} + 2m\delta_y\omega_y\frac{\partial y(t)}{\partial t} + k_y y(t) = L(t) \tag{9}$$

in which m and ω_y respectively represents the mass per unit length and inherent frequency of the film. Substituting Equation (7), we can obtain the following expression:

$$m\frac{\partial^2 y(t)}{\partial t^2} + 2m\delta_y\omega_y\frac{\partial y(t)}{\partial t} + k_y y(t) = \frac{1}{2}\rho U^2 D C_y \tag{10}$$

Since the critical angle of attack is usually a minor value, we can expand the

coefficient of lift C_y at the vicinity of zero via the Taylor series:

$$C_y = C_y(\alpha = 0) + \left[\frac{\partial C_y(\alpha = 0)}{\partial \alpha}\right] \times \alpha + o(\alpha^2)$$

$$= C_L(\alpha = 0) + \left[\frac{\partial C_L(\alpha=0)}{\partial \alpha} + C_D(\alpha = 0)\right] \times \frac{\partial y(t)}{\partial t} \times \frac{1}{U} + 0\left(\frac{\partial y(t)}{\partial t}\right)^2 \quad (11)$$

When the angle of attack α is very small, it's defined as:

$$\alpha = -\frac{\dot{y}(t)}{U} \quad (12)$$

$$\frac{\partial C_y}{\partial \alpha} = \frac{\partial C_L}{\partial \alpha} + C_D \quad (13)$$

The $C_L(\alpha = 0)$ can be neglected during the analysis of situations for vibration, since it is a certain displacement and shall not interfere with the film's vibration. The Equation (10) can thus be derivate as:

$$\frac{\partial^2 y(t)}{\partial t^2} + 2\delta_T \omega_y \frac{\partial y(t)}{\partial t} + \omega_y^2 y(t) = 0 \quad (14)$$

$$2\delta_T \omega_y = 2\delta_y \omega_y + \frac{\rho U^2 D}{2m} \cdot \frac{\partial C_y(\alpha=0)}{\partial \alpha} \quad (15)$$

where δ_T is sum of structural damping and aerodynamic force. The solution of Equation (14) can be expressed as follows:

$$y = A_y e^{-\delta_T \omega_D t} \sin(\omega_D t + \emptyset) \quad (16)$$

in which,

$$\omega_D = \omega_y (1 + \delta_T^2)^{\frac{1}{2}} \quad (17)$$

where A_y represents the initial amplitude and $\emptyset$ is initial phase angle. Based on Equation (16), we can infer that the solution of Equation (14) is steady when $y = 0$. When δ_T changes to a negative number, the steady state of the electrode film would be broken. In this case, the critical vibration condition is achieved according to Den Hartog discriminant. We can attain the following expression after let $\left[\frac{\partial C_L}{\partial \alpha} + C_D\right] = \beta$:

$$\frac{U_y}{f_y D} = \frac{-8\pi m \delta_T}{\rho D^2 \beta} \quad (18)$$

f_y is the inherent frequency of the film, which is calculated as:

$$f_y = \frac{\omega_y}{2\pi} \quad (19)$$

For films with the rectangle cross section, only when β is a negative value and reduced velocity beyond the critical value, the model changes to instability.

Meanwhile, another aerodynamic model in Figure 2f is established to demonstrate torsional stability of the film. In this model, the cross section of the film is approximately regarded as supported by the spring. When the cross section takes

place rotational movement, the angle of attack of inflow will change accordingly. Here, the angle of attack α and relative velocity U_r of the film are expressed as:

$$\alpha = \theta(t) - \tan^{-1}\left(\frac{R\dot{\theta}(t)\sin\gamma}{U + R\dot{\theta}(t)\cos\gamma}\right) \tag{20}$$

$$U_r^2 = \left(R\dot{\theta}(t)\sin\gamma\right)^2 + \left(U + R\dot{\theta}(t)\cos r\right)^2 \tag{21}$$

in which γ is angle between rotation tangent and U, while $\theta(t)$ presents the rotation angle. The angular velocity $\dot{\theta}(t)$ of the structure is defined as:

$$\dot{\theta}(t) = \frac{d_\theta}{d_t} \tag{22}$$

In addition, the torque per unit length is:

$$F_m = \frac{1}{2}pU^2 D^2 C_m \tag{23}$$

where C_m is torsion coefficient that can be defined as:

$$C_m = \frac{U_r^2}{U}C_M \tag{24}$$

C_M is torque factor around the point of rotation, which is attained by wind tunnel tests.

Here, the torsional response force equation of the model is attained as:

$$I_\theta\ddot{\theta}(t) + 2I_\theta\delta_\theta\omega_\theta\dot{\theta}(t) + k_\theta\theta(t) = \frac{1}{2}pU^2 D^2 C_m \tag{25}$$

In which I_θ is polar moment of inertia of the cross section including the fluid's polar mass moment of inertia, δ_θ is structural damping, k_θ is torsional elastic constant per unit length and ω_θ is inherent frequency of the cross section. When the rotation angle is very small, the Equation (20), (21) can be linearized as:

$$\begin{cases} U_r = U \\ \alpha = \theta(t) - \frac{R\dot{\theta}(t)}{U} \end{cases} \tag{26}$$

The linearized relative motion equation is thus definite as:

$$I_\theta\ddot{\theta}(t) + 2I_\theta\delta_\theta\omega_\theta\dot{\theta}(t) + k_\theta\theta(t) = \frac{1}{2}pU^2 D^2 \frac{\partial C_M(\alpha=0)}{\partial\alpha}\left(\theta(t) - \frac{R\dot{\theta}(t)}{U}\right) \tag{27}$$

Then we definite $\varphi = \frac{\partial C_M(\alpha=0)}{\partial\alpha}$, the minimum critical velocity U_θ of torsional instability can be derivate as:

$$\frac{U_\theta}{f_\theta D} = \frac{-8\pi I_\theta\delta_\theta}{\rho D^3 R\varphi} \tag{28}$$

It's inferred that the cross section would rotate clockwise ($\varphi < 0$) and the torque is supposed to decrease, when there exits an instability state. If center of rotating section tends to direction of pressure center, the instable torque would decrease; if center of rotating section moves to the front of pressure center, the model is usually stable. For the film in our TENG device, the air pressure is mainly induced at leading edge of the

film (as have been demonstrated in Figure 2c and Figure S4), and thus the film would trend to instability more easily.

Since vibration of the electrode film in our TENG device is a coupling of galloping and torsion, the motion is two-degree of freedom. The Equation (10) and (25) can further be derivate as:

$$
\begin{cases}
m\ddot{y}(t) + 2m\delta_y\omega_y\dot{y}(t) - S_x\ddot{\theta}(t) + k_y y(t) = \dfrac{1}{2}\rho U^2 D C_y \\[2mm]
I_\theta\ddot{\theta}(t) + 2I_\theta\delta_\theta\omega_\theta\dot{\theta}(t) - S_x\ddot{y}(t) + k_\theta\theta(t) = \dfrac{1}{2}p U^2 D^2 C_m
\end{cases} \tag{29}
$$

Here, S_x is defined as relative displacement (χ, θ) of a point (λ, η) on the vibrating cross section, χ is displacement of the film that perpendicular to inflow and θ is rotation angle. The parameters I_θ, m and S_x are expressed as:

$$
\begin{cases}
I_\theta = \displaystyle\int_A (\lambda^2 + \eta^2)\mu\, d\lambda d\eta \\[2mm]
m = \displaystyle\int_A \mu\, d\lambda d\eta \\[2mm]
S_x = \displaystyle\int_A \lambda\eta\, d\lambda d\eta
\end{cases} \tag{30}
$$

where μ is the mass per unit volume of the film. The angle of attack can be demonstrated by:

$$
\alpha = \theta - \frac{R\dot{\theta}(t)}{U} - \frac{\dot{y}(t)}{U} \tag{31}
$$

Accordingly, we define frequency of principal mode as ω_1 and ω_2, in which

$$
\omega_{1,2} = \frac{\omega_y^2 + \omega_\theta^2 \pm \left[\left(\omega_y^2 + \omega_\theta^2\right)^2 - 4\omega_y^2\omega_\theta^2\left(1 - \dfrac{S_x^2}{I_\theta m}\right) \right]^{\frac{1}{2}}}{2\left(1 - \dfrac{S_x^2}{I_\theta m}\right)} \tag{32}
$$

Here, k_1 and k_2 are given by:

$$
\begin{cases}
k_1 = \dfrac{S_x\omega_1^2}{m\left(\omega_1^2 - \omega_y^2\right)} \\[3mm]
k_2 = \dfrac{S_x\omega_2^2}{I_\theta\left(\omega_2^2 - \omega_\theta^2\right)}
\end{cases} \tag{33}
$$

In this case, the minimum critical velocity U_c of the flow that broke the film's static state can be summarized as:

$$
U_c = \min\left[\frac{-4m\delta_y\omega_y - 4k_2^2 I_\theta\delta_\theta\omega_\theta}{\rho D(Rk_2 + 1)\left(k_2 D\dfrac{\partial C_M}{\partial\alpha} + \dfrac{\partial C_y}{\partial\alpha}\right)}, \frac{-4k_1^2 m\delta_y\omega_y - 4I_\theta\delta_\theta\omega_\theta}{\rho D(R + k_1)\left(k_1\dfrac{\partial y}{\partial\alpha} + D\dfrac{\partial C_y}{\partial\alpha}\right)} \right] \tag{34}
$$

Based on the above aerodynamic models, we can infer that if the velocity of inflow beyond the minimum critical velocity, the input energy worked on the film would be larger than the energy consumed by internal damping of the film. The film

stars to vibrate with growing amplitude, until a balance is reached between input energy and consumed energy by damping. Thus, the film's vibration depends on both parameters of flow flied and the film itself. That is, the deformation performance of the film can be adjusted by modifying these parameters.

Here, since energy collection efficiency is the most important element for our TENG device, some approaches are supposed to be taken to achieve the device's best performance. Under the certain inlet wind energy, the output performance of the device is determined by vibration of the electrode film. Based on Equation (34), various strategies could be developed to enhance vibration of the film, including but not limited to: fabricate lighter materials, decrease elastic modulus of the film, or increase density of the fluid. Among them, introducing perforations on the electrode film could retain optimized geometric parameters while reduce the mass and elastic modulus of the film, which can create prescribed inhomogeneous flow profiles and thus enhance the aeroelastic effect.[28,29]

For the perforations developed on the electrode, several factors of these perforations must be considered: amount, distribution and their diameter. Accordingly, several kinds of systematic tests have been carried out (in the advection of 2.5 m/s), the results are shown in Table S1 and **Figure 3**a.

Firstly, to investigate the influence of perforation amount, we have prepared four electrode films with distinct perforation amount and define them with serial number of "1-1, 1-2, 1-3 and 1-4", respectively. The film without perforation is defined as "0#", as the schematics shown in Table S1. It's inferred that the samples "1-1" and "1-4" have attain better performance, based on change of the film's vibration frequency and amplitude. However, the amount of these perforations on the electrode film should be restricted, since contact area between the electrode film and dielectric layer would decrease sharply with too many perforations, which may weaken the output of the device. Under the circumstances, the case "1-2" with eight perforations is a reasonable choice.

Furthermore, the influence of distribution of these perforations on the electrode film's vibration is investigated. Compared with the regular arrangement in the series "1#", the perforations there are developed to homogeneous interlaced distribution (as series "2#" shown, "2-1, 2-2, 2-3, 2-4"). It's noted that with this interlaced distribution adjustment, a better vibration balance is acquired, as the relationship of vibration frequency and amplitude shown in Figure 3a. That is, though a larger vibration frequency of the electrode film is essential to acquire a multiplied-frequency output, the amplitude of the film can't be ignored. The amplitude directly affects contact area between the AgNWs NFs electrode film and FEP tribo layer. Namely, a too-small vibration amplitude of the film should be modified. Hence, the case "1-2" may be replaced by "2-2" with perforations of interlaced distribution. In addition, the electrode with eight perforations distributed in three rows is also tested, as the case "3-1" shown. It's resulted that the three-row interlaced distribution is unfavorable for the deformation performance of the film, compared to case "2-2" with two-row interlaced distribution.

Accordingly, the dependence on diameter of perforation is experimented, which is

defined as series "4#" ("4-1, 4-2, 4-3"). The performance of samples in series "4#" is desirable, by comparing with series "1#" and "2#". However, the perforation with oversized diameter ("4-3") may be reconsidered, since the fatigue durability of the elastic electrode would be influenced.

Based on the above investigations, the electrode film with optimized distributed perforation are ultimately developed, which are "5-1" and "5-2". As the cases shown, the interval between adjacent perforations in one row is adjusted, where the perforation distribution slightly gathers toward two sides of the film. The overall arrangement of the perforation distribution is somewhat like a transversal letter "S". The adjustment is mainly based on three reasons:

(i) Due to the arched deformation, the middle area of the electrode film would bear a greater stress with the larger deformation. Except the fixed points of the film, the fatigue durability of middle area is also critical. The adjustment of case "5" would relieve potential risk in the middle area of the electrode film.

(ii) With the two arched-shape frameworks, the ventilation volume in the middle cross area of the TENG device is larger than the two sides. To make the electrode film driven by inflow more easily, the side areas of the electrode need to be modified with perforation structure preferentially. From this perspective, the adjustment in "5-1" and "5-2" is also essential, in which the enhanced vibration performance of the film has been acquired (Figure 3a).

(iii) The motion of the electrode film there is the coupling of vortex-induced torsional vibration and galloping, which is different to the single flutter of the non-stretchable film. Hence, the perforation design in case "5" with the distribution shape that likes a transversal letter "S" may enhance the vortex-induced deformation, and thus enhance the compound vibration of the film.

Exhibited in Figure 3b and Movie S5 are the high-speed photograph of comparison between the perforated electrode film (the left side) and an original one (the right side). Clearly can we discover that the film with perforating treatment demonstrates an improved vibration frequency and amplitude. Meanwhile, based on simulation of fluid-structure interactions, vibration performance of the film before and after perforating treatment are also depicted, as shown in Figure 3c, Figure S5 and Movie S6. The results demonstrate that the vibration frequency and amplitude of the electrode film have increased by approximate 20% after developing perforations, which is consistent to the experimental investigation. Figure 3d demonstrates lift curves of the electrode films ((i) ordinary, (ii) with perforations) activated by the airflow. It's noted that convergence time of the film's vibration will reduce 25 % (from 0.4 to 0.3 seconds) with perforated modification, illustrating an improved flow-driven performance. The change of flow field near the perforated electrode film has been exhibited, as the enlarged views shown in **Figure 4**a. The screenshots in the normal size and the dynamic results can be found in the Figure S6 and Movie S7, respectively. Owing to the existence of perforations, fluid interacting with the electrode is more turbulent, contributing to a more drastic deformation. The enlarged views of fluid field near a single perforation are available in Figure 4b. **Figure 5** demonstrates comparison of output performance between the two TENG devices: one

is fabricated with original electrode film, and another with optimized perforated film (in the wind velocity of 2.5 m/s). It is resulted that compared to original TENG device, the device with optimized perforated electrode has a significant enhanced output. Namely, the open-circuit voltage and short-circuit current are both increased by 25%. Accordingly, the overall output power of the device has increased by nearly 56.3%, illustrating the effectiveness of perforated modification on the electrode film to acquire optimized wind energy harvesting device.

Conclusion

In summary, flow-induced vibration behavior of a ultra-stretchable electrode film in TENG device has been studied. The vibration of the ultra-stretchable film is a compound of vortex-induced elastic torsional deformation and pressure-driven galloping. Aerodynamic models based on structural mechanics are established to analyze deformation characteristics of the electrode film, while CFD and simulation of fluid-structure interactions are also introduced. Based on aerodynamic characteristics, perforations are developed on the electrode film as geometric optimization of the TENG device. Fluid interacting with the electrode film is more turbulent with perforated structure modification, in which convergence time of the electrode film's vibration has reduced 25 %, while vibration frequency and amplitude increases by approximate 20%. The open-circuit voltage and short-circuit current of the fabricated TENG are both increased by 25%, that is, the overall output power of the device has increased by nearly 56.3%. This work firstly demonstrates the flow-induced vibration of the ultra-stretchable film in TENG, and may open up a strategy for optimizing current design of wind energy harvesters.

Methods

Fabrication of ultra-thin, ultra-stretchable AgNWs NFs electrode: The unidirectional TPU NFs is prepared using electrospinning (Shenzhen Tong Li Tech Co. Ltd.). Then the TPU NFs are modified by the dilute AgNWs solution (with 0.5% N, N-Dimethylacetamide, by volume). The diameter of used AgNW is 50 nm with length of 100-200 μm. Spin-coating technique is adopted to prepare the Ecoflex film substrate of AgNWs NFs electrode, with thickness around 100 μm. The part A and B of Ecoflex is well stirred with mass ration 1: 1 and cured at vacuum chamber with 40 ºC. The laser ablation based on Engraving machines laser (UNIVERSAL PLS6.75, US) is chosen to develop perforation on the electrode film. The whole size of the electrode film is around 10 cm × 2 cm × 150 μm.

Fabrication of TENG device: 3D printing technology is used to attain arched frameworks of the device, with UV Curable Resin material. The size of arched framework is 10 cm (length) × 2 cm (width), with radian of 0.68 rad. Al coating (with

magnetron sputtering, 300 nm) developed on one surface of FEP films (25 μm) is attached to the two arched substrates, functions as output electrode of negative tribo layer. Finally, the AgNWs NFs electrode is fixed at the middle of the device to form two TENG units.

Characterization and measurement: High speed photography is captured by high-speed camera (Photron, Japan), while the others photographs are attained by ordinary camera (Canon 600D, Japan). Microstructure of the material there is analyzed by SEM (SU8020, Hitachi) and AFM (MFP-3D-SA, Asylum Research). The electrical output of the TENG device is measured by Stanford Research Systems Kethiely 6514.

Acknowledgements

References

(1) Veers, P., Dykes, K., Lantz, E. Grand challenges in the science of wind energy. Science 2019, 366, 443.

(2) Rinne, E., Holttinen, H., Kiviluoma, J., Rissanen, S. Effects of turbine technology and land use on wind power resource potential. Nature Energy 2018, 3, 494.

(3) Spinato, F., Tavner, P.J., Bussel, G.J.W., Koutoulakos, E. Reliability of wind turbine subassemblies. IET Renewable Power Generation. 2009, 3, 387.

(4) Eggleston, D.M., Stoddard, F. Wind Turbine Engineering Design. OSTI.GOV: New York, 1987.

(5) Jonkman, J., Butterfield, S., Musial, W., Scott, G. Definition of A 5-MW Reference Wind Turbine for Offshore System Development. OSTI.GOV: New York, 2009.

(6) Spera, D A. Wind Turbine Technology. OSTI.GOV: New York, 1994.

(7) Hau, E. Wind Turbines: Fundamentals, Technologies, Application, Economics. Springer Science & Business Media: Berlin, 2013.

(8) Wright, A.K., Wood, D.H. The starting and low wind speed behaviour of a small horizontal axis wind turbine. Journal of Wind Engineering and Industrial Aerodynamics. 2004, 92, 1265.

(9) Fan, F., Tian, Z., Wang, Z.L. Flexible triboelectric generator. Nano Energy. 2012, 1, 328-334.

(10) Wang, Z.L., Chen, J., lin, L. Progress in triboelectric nanogenerators as a new

energy technology and self-powered sensors. Energy Environ. Sci. 2015, 8, 2250-2282.

(11) Hinchet, R., Yoon, H. J., Ryu, H., Kim, M. K., Choi, E. K., Kim, D. S., Kim, S. W. Transcutaneous ultrasound energy harvesting using capacitive triboelectric technology. Science. 2019, 365, 491−494.

(12) Seung, W., Yoon, H. j., Kim, T. Y., Ryu, H., Kim, J., Lee, K. J., Shin, K. S. Park, Y. K., Park, Y. J., Kim, S. W. Nanogenerators: Boosting Power‐Generating Performance of Triboelectric Nanogenerators via Artificial Control of Ferroelectric Polarization and Dielectric Properties. Adv. Energy Mater. 2017, 7, 1600988.

(13) Bae, J.Y., Lee, J., Kim, S.M., Ha, J., Lee, B.S., Park, Y.J., Choong, C., Kim, J.B., Wang, Z.L., Kim, H.Y., Park, J.J., Chung, U.I. Flutter-driven triboelectrification for harvesting wind energy. Nat. Commun 2014, 5, 4929.

(14) Li, X., Jiang C., Zhao, F., Shao, Y., Ying Y., Ping, J. A self-charging device with bionic self-cleaning interface for energy harvesting. Nano Energy. 2020, 73, 104738.

(15) Pang, Y., Chen, S., Chu, Y., Wang, Z.L., Cao, C. Matryoshka-inspired hierarchically structured triboelectric nanogenerators for wave energy harvesting. Nano Energy. 2019, 66, 104131.

(16) Ren, Z., Ding, Y., Nie, J., Wang, F., Xu, L., Lin, S., Chen, X., Wang, Z.L. Environmental Energy Harvesting Adapting to Different Weather Conditions and Self-Powered Vapor Sensor Based on Humidity-Responsive Triboelectric Nanogenerators. ACS Appl. Mater. Interfaces. 2019, 11, 6143.

(17) Kim, S., Gupta, M. K., Lee, K. Y., Sohn, A., Kim, T. Y., Shin, K. S. Kim, D., Kim, S. K., Lee, K. H., Shin, H., Kim, D. W., Kim, S. W. Transparent Flexible Graphene Triboelectric Nanogenerators. Adv. Mater. 2014, 26, 3918.

(18) Khan, U., Kim, T. H., Ryu, H., Seung, W., Kim, S. W. Graphene Tribotronics for Electronic Skin and Touch Screen Applications. Adv. Mater. 2017, 29, 1603544.

(19) Wang, S., Mu, X., Wang, X., Gu, A.Y., Wang, Z.L., Yang, Y. Elasto-aerodynamics-driven triboelectric nanogenerator for scavenging air-flow energy. ACS Nano. 2015, 9, 9554-9563.

(20) Ren, Z., Nie, J., Shao, J., Lai, Q., Wang, L., Chen, J., Chen, X., Wang, Z.L. Fully Elastic and Metal-Free Tactile Sensors for Detecting both Normal and Tangential Forces Based on Triboelectric Nanogenerators. Adv. Funct. Mater. 2018, 28, 1802989.

(21) Li, X., Jiang C., Zhao, F., Lan, L., Yao, L., Yu, Y., Ping, J., Ying Y. Fully stretchable triboelectric nanogenerator for energy harvesting and self-powered sensing. Nano Energy. 2019, 61, 78-85.

(22) Ren, Z., Wang, Z., Liu, Z., Wang, L., Guo, H., Li, L., Li, S., Chen, X., Tang, W., Wang, Z.L. Energy Harvesting from Breeze Wind (0.7–6 m s^{-1}) Using Ultra-Stretchable Triboelectric Nanogenerator. Adv. Energy Mater. 2020, 10, 2001770.

(23) Quan, Z.C., Han, C.B., Jiang, T., Wang, Z.L. Robust thin films‐based triboelectric nanogenerator arrays for harvesting bidirectional wind energy. Adv. Energy Mater. 2016, 6, 1501799.

(24) Guo, H., He, X., Zhong, J., Zhong, Q., Leng, Q., Hu, C., Chen, J., Tian, L., Xia,Y., Zhou, J. A nanogenerator for harvesting airflow energy and light energy. J. Mater. Chem. A, 2014, 2, 2079.

(25) Zhang, L., Zhang, B.B., Chen, J., Lin, L., Deng, W., Tang, J., Zhang, H., Pan, H., Zhu, M., Yang, W., Wang, Z.L. Lawn Structured Triboelectric Nanogenerators for Scavenging Sweeping Wind Energy on Rooftops. Adv. Mater. 2016, 28, 1650.

(26) Lin, H., He, M., Jing, Q., Yang, W., Wang, S., Liu, Y., Zhang, Y., Li, J., Li, N., Ma, Y., Wang, L., Xie, Y. Angle-shaped triboelectric nanogenerator for harvesting environmental wind energy. Nano Energy. 2019, 56, 269-276.

(27) Wang, J., Ding, W., Pan, L., Wu, C., Yu, H., Yang, L., Liao, R., Wang, Z.L. Self-powered wind sensor system for detecting wind speed and direction based on a triboelectric nanogenerator. ACS Nano. 2018, 12, 3954−3963.

(28) Caldas, L. C., Behn, M., Tapken, U. Experimental study of noise generation due to flow through perforated plates. DAGA 2019 Rostock.

(29) Gunn, E. J., Hall, C. A. ASME. Aerodynamics of boundary layer ingesting fans. Turbo Expo: Power for Land, Sea, and Air, GT2014-26142, V01AT01A024.
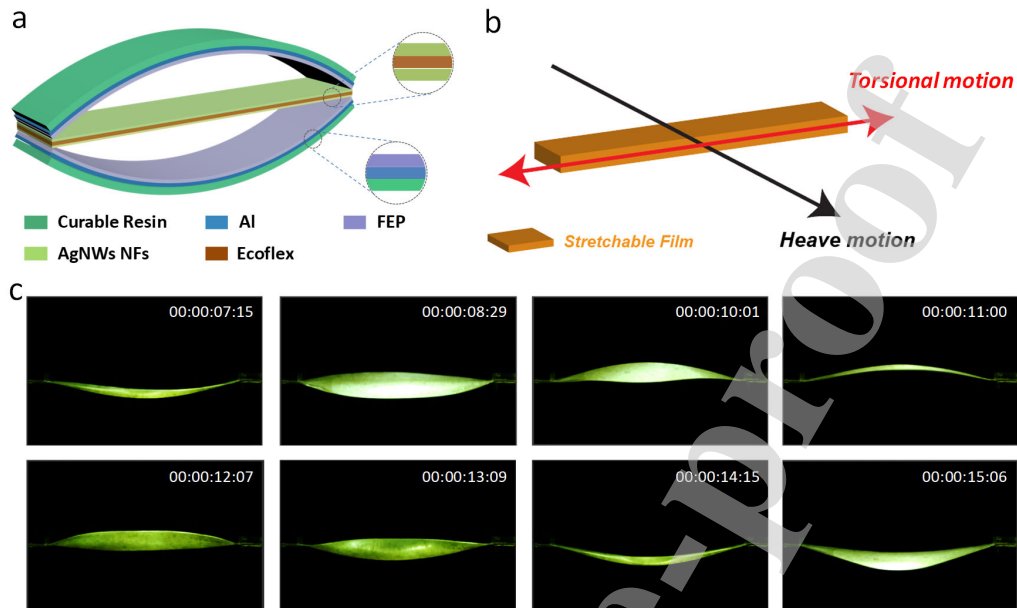
Figure 1. Design of the TENG and deformation characteristic of the ultra-stretchable electrode film. (**a**). Structure and materials design of the TENG. (**b**). Schematic diagram of compound deformation of the ultra-stretchable AgNWs NFs film in the wind flow. (**c**). High speed photography of the ultra-stretchable AgNWs NFs film vibrating in the flow. Inset in the top right-hand corner is the corresponding step time.
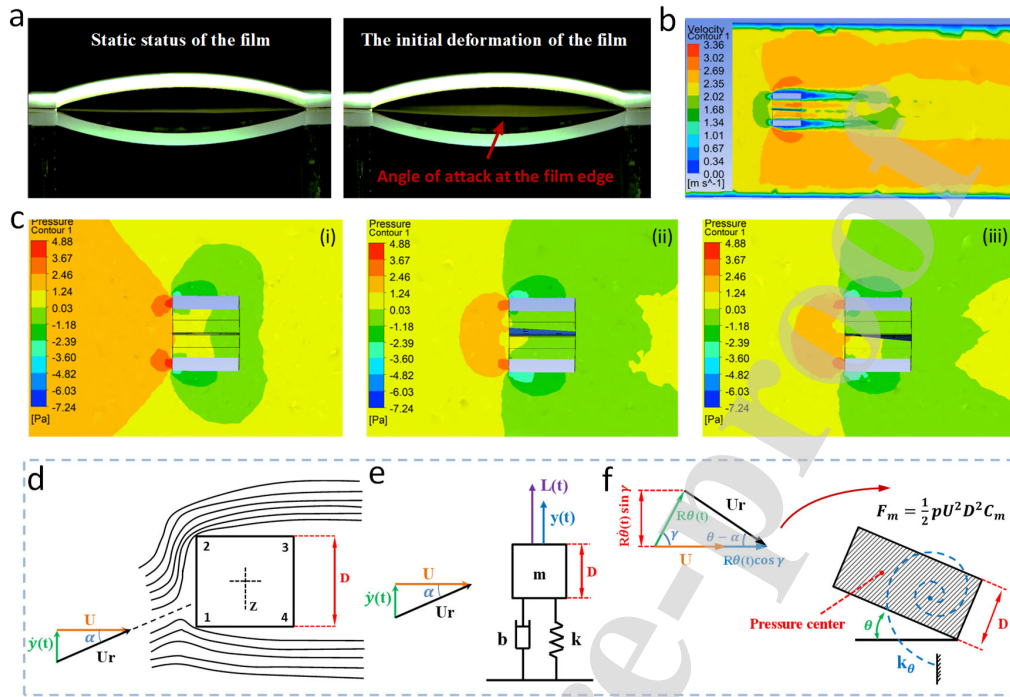
Figure 2. Vibration mechanism and motivation of the electrode film. (**a**). Status of the film electrode changing from static to vibration under wind flow. (**b**). Screenshot from ANSYS exhibiting vortexes shedding from the trailing edge of the film at the initial state under wind flow. (**c**). Pressure distribution change of the film at the beginning of the flow-induced vibration. (**d,e,f**). The aerodynamic models of the film in flow field.
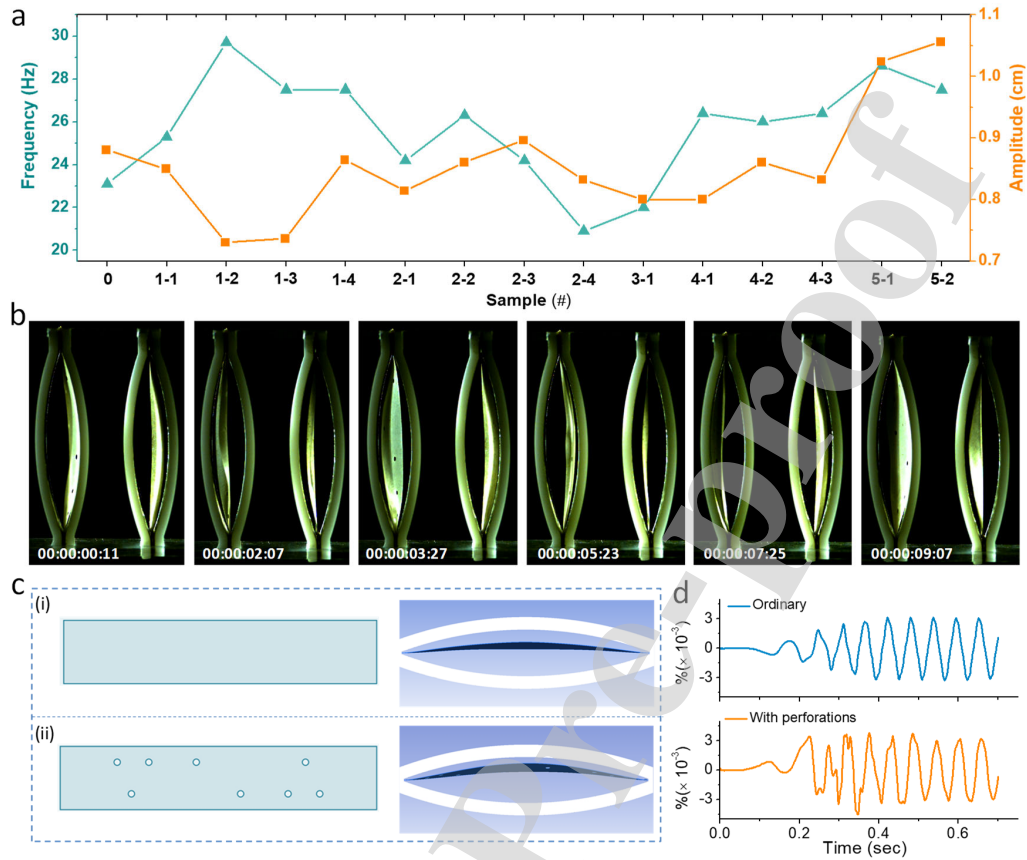
Figure 3. Design and optimization of perforations developed on the electrode film. (**a**). Vibration amplitude and frequency of the electrode with distinct distributed perforations. (**b**). High speed photography of vibrations of the perforated (left) and ordinary (right) electrode films. Inset in the bottom left is the corresponding step time. (**c**). The maximum amplitude and (**d**) convergence curves of two distinct electrode films.
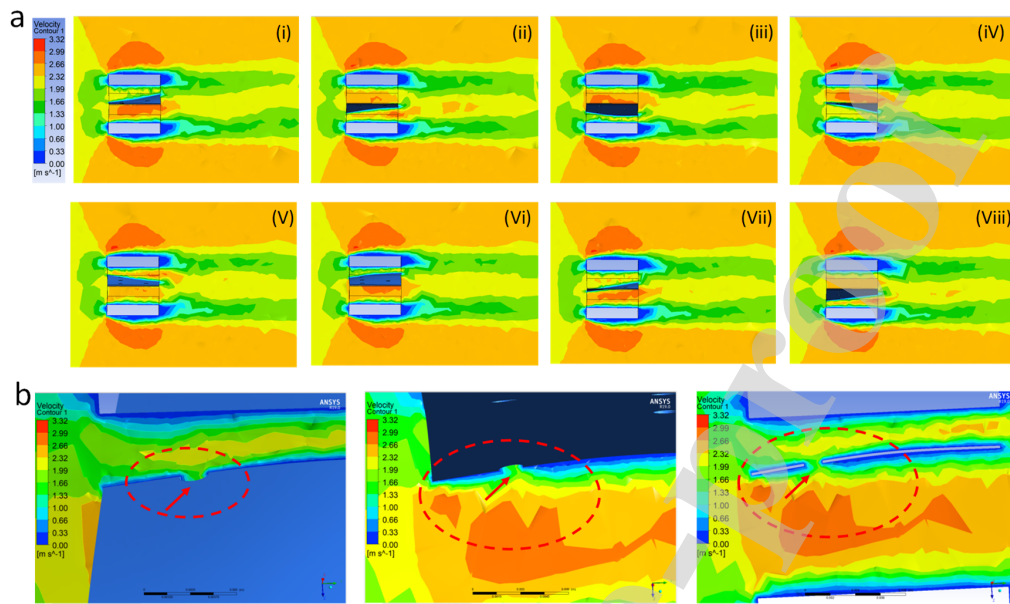
Figure 4. Flow field distribution near surfaces of the perforated electrode film. (**a**). The changing flow field near the perforated electrode film (side view). (**b**). Flow field around a perforation on the film.
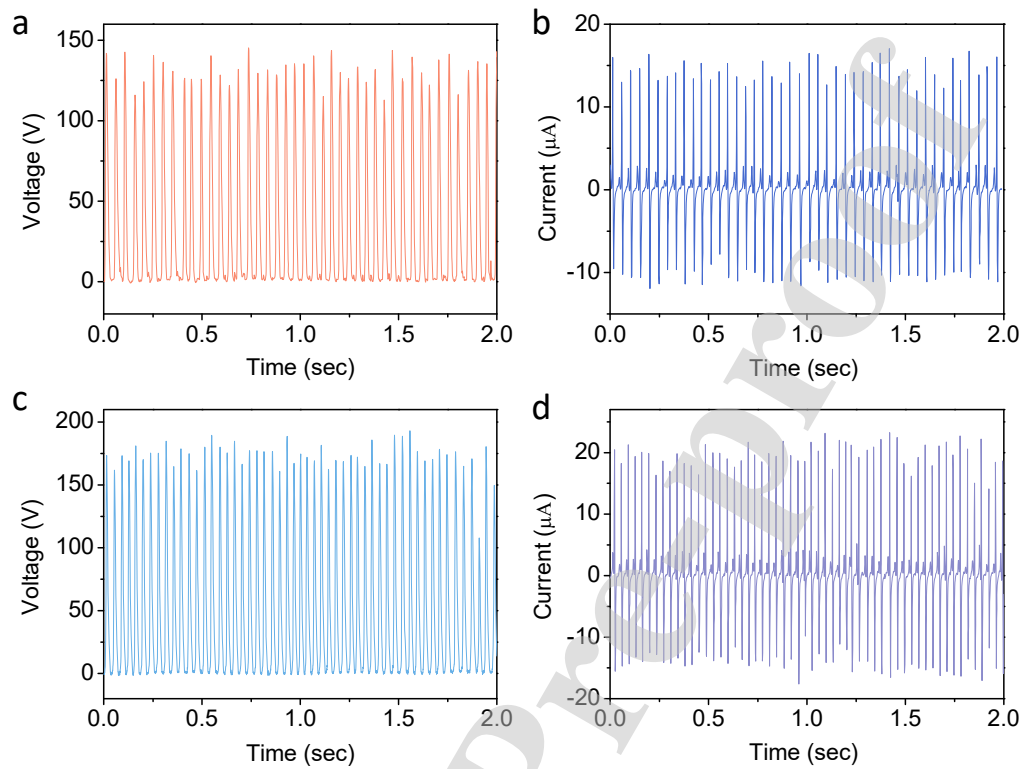
Figure 5. Output performance of the TENG devices. (**a**). Dependence of open-circuit voltage and (**b**) short-circuit current of TENG device fabricated with original electrode film, under the flow velocity 2.5 m/s. (**c**). Dependence of open-circuit voltage and (**d**) short-circuit current of TENG device fabricated with perforated electrode film, under the flow velocity 2.5 m/s.

Conflict of Interest

The authors declared that they have <u>no</u> conflicts of interest to this work.